

Role of Electrostatics in Modulating Hydrophobic Interactions and Barriers to Hydrophobic Assembly

Brad A. Bauer and Sandeep Patel*

Department of Chemistry and Biochemistry, University of Delaware, Newark, Delaware 19716

Received: March 5, 2010; Revised Manuscript Received: April 20, 2010

Hydrophobic effects continue to be an active area of research due to implications for a wide range of physicochemical phenomena. Molecular dynamics simulations have been used extensively in the study of such effects using various water potential models, with few studies addressing the differences between models. In particular, studies considering the explicit treatment of water polarizability are underrepresented in the literature. We present results from molecular dynamics simulations that systematically compare the dependence of large-scale hydrophobic effects on the water model. We consider three common nonpolarizable models (SPC/E, TIP3P, and TIP4P) and two common polarizable models (TIP4P-FQ and SWM4-NDP). Results highlight the similarities and differences of the different water models in the vicinity of two large hydrophobic plates. In particular, profiles of average density, density fluctuations, orientation, and hydrogen bonding show only minor differences among the water models studied. However, the potential of mean force for the hydrophobe dimerization is significantly reduced in the polarizable water systems. TIP4P-FQ shows the deepest minimum of approximately $-54(\pm 3)$ kcal/mol compared to $-40(\pm 3)$, $-40(\pm 2)$, $-42(\pm 3)$, and $-45(\pm 5)$ kcal/mol for TIP4P, TIP3P, SPC/E, and SWM4-NDP (all relative to the dissociated state). We discuss the relationship between hydrophobic association and the strength of water–water interactions in the liquid phase. Results suggest that models treating polarizability (both implicitly and explicitly) influence a stronger driving force toward hydrophobic assembly. Implications of these results, as well as prospectives on future work, are discussed.

I. Introduction

Hydrophobic effects play an important role in many natural phenomena including processes ranging from the observed separation of oil/water mixtures, protein folding, and the aggregation and self-assembly of hydrophobic entities such as micelles, bilayers, and monolayers.^{1–14} Theoretical investigations and molecular simulations regarding the nature, origins, and manipulation of this effect have enjoyed a long history.^{6,10,12,13,15–34} Early simulation studies focused on describing the hydration of small molecules such as methane and noble gases.^{17,35–43} Numerous studies have considered potentials of mean force for the association of hydrophobic, nonpolar moieties in various solvents modeled using different force fields. Lum, Chandler, and Weeks developed a theoretical framework for describing the hydrophobic effect on the molecular scale (LCW theory).²¹ The LCW theory and corroborating molecular dynamics simulations suggest a length-scale dependence for the nature of hydrophobic interactions. For small solutes, water is capable of undergoing slight distortions in the hydrogen bond network to accommodate the solvation of the solute. However, large solutes can significantly disrupt the hydrogen bond network. In particular, rather intriguing notions of increased probabilities of empty volume (voids) coupled to long-range water–water correlations near hydrophobic surfaces have come to the forefront to consider the water–hydrophobe interface on a similar footing as the water liquid–vapor interface.^{44–47}

The use of simplistic model systems such as hydrophobic plates of varying sizes and roughness^{24,48–54} to address the fundamental mechanistic view of the hydrophobic effect has resurged in the recent literature.⁴⁵ In the study of water confined between or within large scale hydrophobes (carbon nanotubes,

hydrophobic plates, hydrophobic pockets), a wetting/dewetting transition is often observed. Simulations by Hummer et al.^{20,55} have shown water to form single-layer hydrogen-bonded strings which transfer water through a carbon nanotube in pulses. Simulations by Zangi and Berne demonstrate the dewetting of a region confined between two hydrophobic plates.²⁴ Below a certain critical distance (d_c), water between two plates becomes unstable and evacuates the confined volume, while above this critical distance water is capable of forming stable hydrogen bond networks and existing favorably between the plates. Similar behavior is observed for simulations in which the water clusters are confined within a hydrophobic cavity–ligand system.^{56,57} As one would expect, the strength of water–plate interaction affects wetting, and such effects have been probed directly by variation of interaction parameters.⁵⁸ In many cases, the strength of water–water interactions has not been directly considered with regard to its effects on association of large hydrophobes. Indirectly, through the use of different water potentials, one can discern that there are no qualitative differences in the picture of hydrophobic interactions that arise from these studies.

Though numerous studies employing molecular simulations with today's state-of-the-art fixed-charge (additive) electrostatic models have appeared in the literature, there are relatively few studies of such effects on large hydrophobes using force fields that can modulate the molecular electrostatics in response to local environment, that is, polarizable or nonadditive electrostatic force fields. The varying nature of electrostatics of water molecules in the condensed phase, at the liquid–vapor interface, and near hydrophobic and hydrophilic surfaces is dictated by quantum effects.^{59,60} Fixed-charge force fields are not able to capture this effect explicitly, stimulating questions about the implications of electrostatic polarization. For instance, one can consider the variation of the dipole moment of water in the low-

* Corresponding author. E-mail: sapatel@udel.edu.

density (rarefied) regions between hydrophobic surfaces as the surfaces near one another; the nature of the water dipole moment near the surface also differs from the bulk phase, and this is evident from variations in density and environment effects in the anisotropic environment of a hydrophobe–solvent interface. A further subtlety arises when one considers that the nature of polarizability itself is dynamic. Substantial recent work on the nature of water polarizability in condensed phases has demonstrated not only that the intrinsic polarizability of water molecules decreases in the condensed phase but also that there is a dependence on the local hydrogen bonding structure of the water molecule.⁶¹ With these ideas in mind, we consider in this article the effects of varying solvent electrostatics on the hydrophobic interactions of large surfaces. We adopt additive models previously used to study such systems and nonadditive (polarizable) models to present a systematic comparison. Regarding polarizable force fields currently pursued, force fields implementing Charge Equilibration (CHEQ),^{62–67} Drude-Oscillators,^{68–73} and Point-Dipole^{74–79} approaches to model polarizability are becoming increasingly popular, particularly enabled by advances in modern computational resources. Few studies on hydrophobic effects consider explicit treatment of polarizability.^{38,41,42} Furthermore, these studies consider hydrophobic effects using small molecule hydrophobes (i.e., methane), without consideration of solvent polarizability effects on large-scale hydrophobic interactions. Thus, in this study, we consider the potential of mean force between two large hydrophobic plates as has been previously studied using nonpolarizable force fields by Zangi et al.²⁴ We consider several nonpolarizable water force fields, as well as two polarizable water force fields, the TIP4P-FQ and SWM4-NDP water models. The former is based on the charge equilibration formalism and the latter on the Drude oscillator model. Both force fields are implemented in the CHARMM molecular modeling package. In Section II, we detail our methods and force fields. In Section III, we consider several properties of water in the vicinity of the hydrophobes, as well as the potential of mean force for association of the hydrophobes. In Section IV, we present further discussion and conclusions.

II. Methods

Molecular dynamics simulations were performed in the canonical ensemble (*NVT*) using the CHARMM molecular modeling program.⁸⁰ Figure 1 shows the system used in this study. Each system consisted of two carbon plates hydrated with 4538 water molecules in a $36 \times 36 \times 200$ Å box. Two liquid–vapor (LV) interfaces were present in the *z*-direction; however, at least 25 Å of bulk water phase separated the LV interfaces from the water–plate (WP) interfaces, minimizing the effect of the LV interface on WP properties. The effect of this geometry on computed potentials of mean force was assessed through results of the PMF for plates solvated in the SPC/E water model for which previous work by Zangi et al. provides reference PMF; this control will be discussed below in Section III.B. Water molecules were represented by each the TIP3P,⁸¹ TIP4P,⁸¹ SPC/E,⁸² TIP4P-FQ,⁶³ and SWM4-NDP⁷⁰ models, and the latter two are polarizable models. Each plate consisted of 31 atoms arranged in a triangular lattice with bond length of 3.2 Å. The plate atoms were each assigned Lennard-Jones parameters of $R_{\min} = 4.4898$ Å and $\epsilon = 0.1195$ kcal/mol; however, interactions among atoms on the same plate were excluded.²⁴ Interactions between plates and water were fixed to reproduce the combined interaction of SPC/E water and the plates ($R_{\min} = 4.022$ Å and $\epsilon = 0.1362$ kcal/mol); this set of

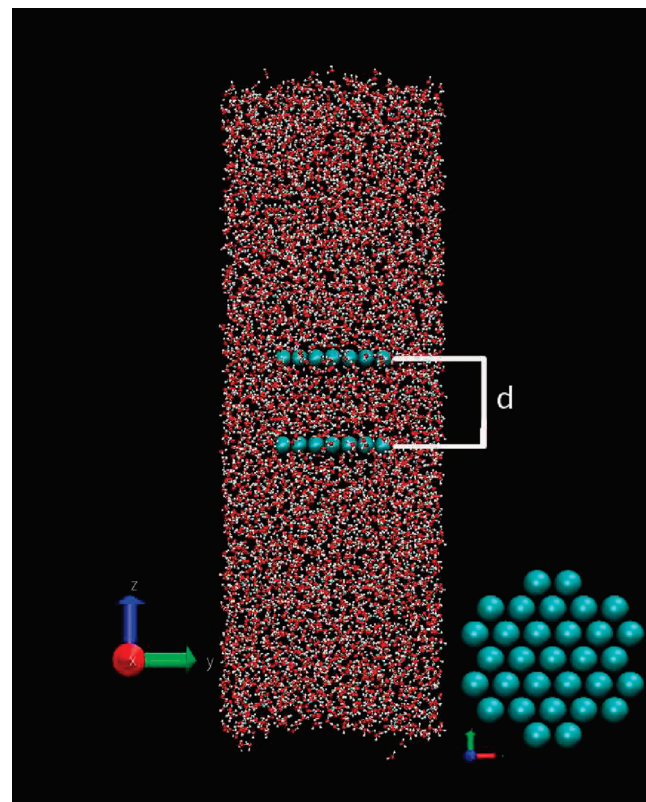


Figure 1. System used in this study. The *z*-direction is normal to the plate–water and water–air interface; *d* denotes the distance between the *z*-component of the center of mass of the two plates. The water slab length is approximately 110 Å, and *d* is varied between 3.6 and 14.4 Å. The plate geometry in the *xy*-plane is shown in the lower right corner.

parameters has previously been shown to adequately reproduce the interaction between water and a hydrocarbon monolayer.^{83,84} Parameters used to model water–water, water–plate, and plate–plate interactions are summarized in Table 1. We emphasize that interactions involving plates (plate–plate and plate–water) are the same in all systems studied, allowing for a direct comparison of the influence of different water models on the large-scale hydrophobic effect. The plates were held in registry with respect to each other, and the positions of all plate atoms were held fixed throughout the course of the simulation. The plate–plate distance was varied from 3.6 to 14.4 Å in the *z*-direction, with about 30 distances sampled for each model. Each distance was sampled for at least 2 ns, although sampling was increased near the critical point where convergence is slow due to fluctuations associated with wetting and dewetting.

Regarding the functional forms of the interactions used in this study, dispersion–repulsion interactions were treated with a standard Lennard-Jones “12-6” potential

$$E_{\text{LJ}} = \sum_{ij} \epsilon_{ij} \left(\frac{R_{\min,ij}^{12}}{r_{ij}^{12}} - 2 \frac{R_{\min,ij}^6}{r_{ij}^6} \right) \quad (1)$$

with summation running over all nonbonded pairs. Electrostatic interactions between each pair of atoms located on different molecules were treated with a standard Coulomb potential

$$E_{\text{Coulomb}} = \frac{1}{2} \sum_{i=1}^{MN} \sum_{j=1}^{MN} \frac{Q_i Q_j}{r_{ij}} \quad (2)$$

TABLE 1: Nonbond Parameters for Oxygen–Oxygen, Oxygen–Plate, and Plate–Plate Interactions Used in This Study^a

model	O–O		O–plate		plate–plate		Q_O	Q_H
	ϵ (kcal/mol)	R_{\min} (Å)	ϵ (kcal/mol)	R_{\min} (Å)	ϵ (kcal/mol)	R_{\min} (Å)		
TIP3P	0.1521	3.536	0.1362	4.022	0.1195	4.490	-0.8340	0.4170
TIP4P	0.1550	3.540	0.1362	4.022	0.1195	4.490	-1.0400	0.5200
SPC/E	0.1554	3.553	0.1362	4.022	0.1195	4.490	-0.8476	0.4238
SWM4-NDP	0.2109	3.574	0.1362	4.022	0.1195	4.490	-1.11466	0.55733
TIP4P-FQ	0.2862	3.546	0.1362	4.022	0.1195	4.490	-0.8880	0.4440

^a Charges on oxygen and hydrogen sites for water are also included; the oxygen charges for TIP4P, TIP4P-FQ, and SWM4-NDP denote the charges on the *M*-site. Charges on the plate atoms were set to zero. Lennard-Jones interactions between atoms within a plate were set to zero. We use the TIP3P model parameterized for CHARMM. This model features an additional Lennard-Jones site on the H ($R_{\min} = 0.449$ Å and $\epsilon = 0.046$ kcal/mol), which was included for all TIP3P water interactions; interactions between plates and hydrogen were turned off. Charges presented are for the gas phase. Charges equal and opposite in magnitude $|Q| = 1.7164$ were placed on the oxygen and the Drude sites (the latter of which received the negative charge).

Within the Charge Equilibration formalism used to simulate the TIP4P-FQ systems, the electrostatic energy also includes contributions from intramolecular interactions in an *N*-atom molecule

$$E_{\text{CHEQ}}(Q) = \sum_{i=1}^N \left(\chi_i Q_i + \frac{1}{2} \eta_i Q_i^2 \right) + \sum_{i < j}^N Q_i Q_j J_{ij} + \lambda \left(\sum_{i=1}^N Q_i - Q_{\text{total}} \right) \quad (3)$$

Here, χ and η represent the atomic electronegativity and hardness which control the directionality and resistance to flow of charge, respectively. The term J_{ij} is the interatomic hardness. Charge neutrality is enforced in the last term via a Lagrange multiplier. We remark that the SWM4-NDP model is rooted in the Drude-formalism, in which atomic charges are fixed and dipoles are induced via the displacement of a charged Drude particle.

Long-range electrostatic contributions were treated using particle-mesh Ewald (PME)⁸⁵ with approximately 1 Å fft grid spacing and a screening parameter $\kappa = 0.330$. Nonbonded interactions were gradually truncated to zero from 11 to 12 Å. Simulation temperature was maintained at 300 K using a Nose–Hoover thermostat. The rigid molecular geometry of each water molecule was maintained using SHAKE.⁸⁶ For simulations involving TIP4P-FQ water, fictitious charge degrees of freedom were assigned masses of 0.000069 kcal/(mol ps²). These charge degrees of freedom were coupled to a thermostat at 1 K with a mass of 0.005 kcal/(mol ps²) using the Nose–Hoover⁸⁷ method. The classical equations of motion for TIP4P-FQ, TIP4P, SPC/E, and TIP3P were propagated using the Verlet leapfrog integrator; SWM4-NDP was propagated using the Velocity-Verlet integrator. Time steps of 1.0 fs were used for SPC/E, TIP3P, TIP4P, and SWM4-NDP, while a 0.5 fs time step was used for TIP4P-FQ.

Unless otherwise stated, position-dependent profiles are in the *z*-direction (normal to the plate–water interface). Particular emphasis is placed on water in the vicinity of the hydrophobic plates, especially those molecules confined between plates. Therefore, we restrict sampling for *z*-dependent profiles to a cylinder of $r = 8.0$ Å about the center of the plates. The choice of this radius is based on the work of Zangi and Berne²⁴ from which our plate geometries are taken. We remark that use of a smaller radius affects the relative number of confined water molecules at each separation distance but ultimately has minimal effect on the qualitative behavior of the interior water count (and its implications for wetting/dewetting transitions). Fur-

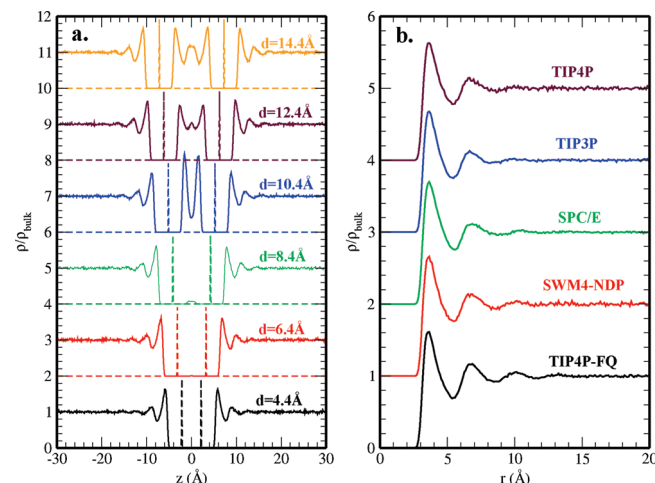


Figure 2. Average density profiles along the *z*-direction (normal to the plate–water interface). (a) Variation of the SWM4-NDP density profile with increasing plate–plate separation distance. Plate positions are denoted as dashed vertical lines. (b) Density profiles for different water models as a function of *z*-position relative to the *z*-component of the plate center of mass. Vertical shifts of 2 and 1 units were imposed for panels a and b, respectively.

thermore, we consider several properties as a function of the plate–plate separation distance, d , which represents the distance between the *z*-center of mass component of the plates.

III. Results

A. Density Profiles. In the vicinity of purely repulsive hydrophobic surfaces, water is believed to have monotonically decreasing density similar to the liquid–vapor interface.⁴⁶ The inclusion of dispersion interactions (as considered in the present study) allows for water to occupy space close to the plates more readily. We consider density profiles as a function of the position along the *z*-direction normal to the plate–water interface. Figure 2a shows the density of SWM4-NDP water at varying plate–plate separation distances ranging from 4.4 Å (near-contact) to 14.4 Å (fully separated plate–plate distance). The choice of SWM4-NDP for this analysis is arbitrary, however, since all models investigated show similar behavior. Figure 2b explicitly considers differences in the water density profiles as a function of the *z*-position relative to the *z*-component of the plate center of mass. Similar behavior is observed for all models, although we note TIP4P-FQ features slightly enhanced structure in the vicinity of the plates (evident by a more pronounced first maximum and minimum).

The water–hydrophobe interface is rapidly changing, and additional analysis involving the fluctuations in density helps

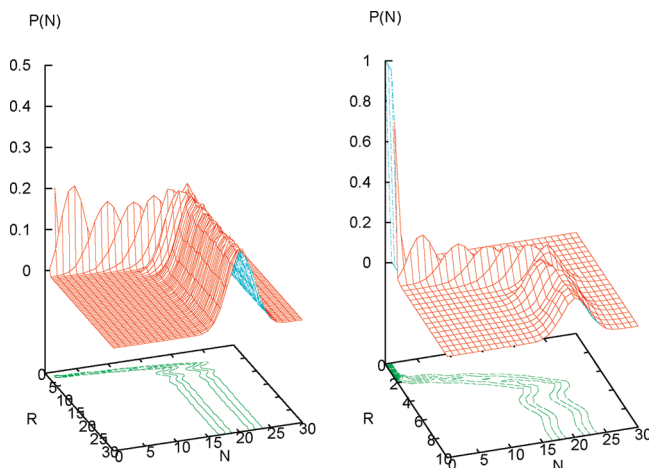


Figure 3. 3-Dimensional probability distribution for finding N water molecules within a cylindrical sampling region ($w = 3.0 \text{ \AA}$ and $r = 8.0 \text{ \AA}$) positioned at a distance R from the plate. Left panel demonstrates this probability distribution extending 30 \AA into the bulk region. The right panel is a closer view of this distribution in the vicinity of the water–hydrophobe surface.

illuminate the complete picture of water density in this region.⁴⁶ Studies by Patel et al.⁴⁶ and Godawat et al.⁴⁵ demonstrate that water density fluctuations increase at a hydrophobic interface using biased sampling methods in conjunction with the Weighted Histogram Analysis Method (WHAM). Patel et al.⁴⁶ show that water density fluctuations in probe volumes adjacent to a hydrophobic interface within an aqueous environment are higher relative to a hydrophilic interface in the same environment. Godawat et al.⁴⁵ calculate probability distributions of occupancy of probe volumes in the vicinity of functionalized self-assembled monolayers and find for the distribution an increasing deviation from Gaussian behavior with increasing hydrophobicity of the functional group. To investigate the density fluctuations for each water model near the plates, we consider the probability ($P_v(N)$) of finding N water molecules (specifically the oxygen atom) within a given sampling volume (v). The sampling volume was taken as a disk of radius 8.0 \AA and width 3 \AA that was aligned with the plate in the z -position; the distance (R) between the center of the plates and the center of the sampling volume was varied using 0.5 \AA increments. This allows us to view a 3-dimensional probability distribution for finding N molecules in the sampling volume at a given distance position normal to the water–hydrophobe interface (Figure 3). The contour plots for the probability surface are shown in Figure 4a. All water models demonstrate similar qualitative behavior. In the region of approximately $0\text{--}2 \text{ \AA}$ (within the excluded volume of plate atoms), we observe an obvious unit probability of observing empty sampling volumes. Just beyond this distance, the number of water molecules within the volume increases in agreement with the average density profiles of Figure 2b. Within the bulk region, the probability profiles become indistinguishable with changes in the z -position of the sampling region. A more quantitative comparison among models can be obtained from the comparison of the standard deviation of this distribution as a function of position sampled. We use the standard deviation from these distributions as a metric to gauge the fluctuations of water density based on the proximity to the hydrophobic interface; such fluctuations have been shown to correlate to the strength of the hydrophobic interaction.^{45,46} The standard deviations are expressed relative to the bulk value for each model. Although the bulk values were comparable among models, the $\sigma_{\rho,\text{bulk}}$ was slightly lower for the polarizable models (~ 2.1

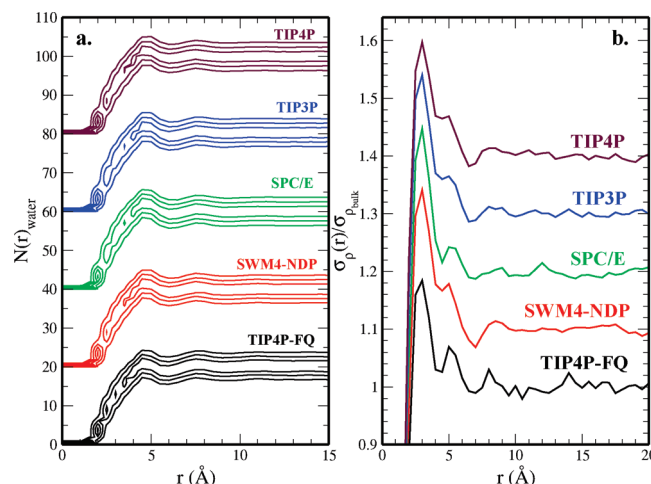


Figure 4. Analysis of density fluctuations in the vicinity of plates. (a) Contour plots for the probability distribution of finding N water molecules within a sampling disk located at a given distance r from the plate extending into the bulk region. Results for each model were offset by 20 vertical units. (b) Standard deviations of these probability distributions as a function of position of sampling disk (normalized to the bulk value). This quantity represents a metric of enhanced density fluctuations in the vicinity of the plate. Results are offset by 0.1 vertical units.

compared to ~ 2.2), which can be attributed to lower self-diffusion constants and isothermal compressibilities for these models. Within the error associated with the data, all models show similar density fluctuation enhancement (relative to the bulk). This is expected since the strength of the plate–water interaction is the same for all models.

With focus on observing a wetting/dewetting transition for a critical plate separation distance, the number of water molecules confined between the two plates as a function of plate–plate separation distance (d) is shown in Figure 5a. Water molecules whose oxygen atom was within $r_{xy} < 8.0 \text{ \AA}$ from the origin and $|z| < d/2$ were included. Plate–plate distances of approximately $9.6\text{--}10.6 \text{ \AA}$ comprise the critical region since the confined volume experiences the greatest change in water density between these distances. The TIP4P-FQ water model shows the most gradual transition from fully filled to fully unfilled states of the five water models studied. This suggests a broad range of plate–plate distances where both filled and unfilled states coexist. At these plate separations, significant fluctuations in the density of the confined region are manifest. We consider these next.

The critical distance represents a thermodynamic stability limit in which an equal probability of filled and unfilled states exists. To this end, we explicitly consider such probabilities over a range of separation distances for TIP4P-FQ, SWM4-NDP, and SPC/E in Figure 5b, c, and d, respectively. For distances less than the critical point, low density/vacant states are prevalent, whereas filled states dominate above this point. By integrating the area under each distribution we can estimate the probability of filled and unfilled states for each distance. These probabilities can then be interpolated to find the point at which probability of a filled state equals the probability of an unfilled state or, equivalently, a fluctuation based estimation of the critical distance. The critical distances predicted by this approach are approximately $9.7, 9.8, 9.9, 9.9$, and 10.5 \AA for the SPC/E, TIP3P, TIP4P, SWM4-NDP, and TIP4P-FQ, respectively. These values are in qualitative agreement with the distances in which the average interior water count sharply increases.

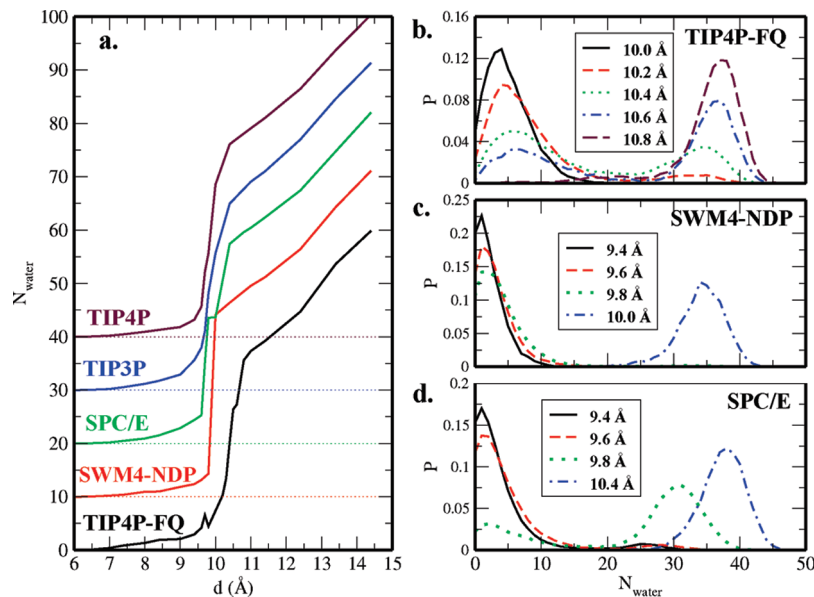


Figure 5. Water between plates. (a) Average number of water molecules between plates as a function of separation distance for all water models studied. A vertical offset of 10 is imposed for clarity. The distribution of number of water molecules between plates in the critical region for (b) TIP4P-FQ, (c) SWM4-NDP, and (d) SPC/E.

The critical distance differs among models despite implementing the same water–plate interactions. This suggests that the polarizable TIP4P-FQ model requires a larger plate–plate separation to fill/wet the interior region than is observed for the other models; filled states in the critical region of distances are less stable thermodynamically for the TIP4P-FQ than for the other models. Furthermore, the TIP4P-FQ water model accommodates a much softer transition compared to all nonpolarizable models and even the polarizable SWM4-NDP water model. This is a consequence of the broader distribution of charges and, thus, dipole moments of the TIP4P-FQ water model compared to the SWM4-NDP force field. The broader distribution of electrostatic environments accommodates the coexistence of filled and unfilled states; because water molecules can more easily adopt electronic configurations that are less polar than the average, unfilled states are more easily stabilized, and thus such states more easily compete with filled states. Specifically, the standard deviation of the dipole moment distribution of bulk TIP4P-FQ water is 0.2 D, whereas that of SWM4-NDP is 0.16 D; the present results suggest that a difference of this magnitude is sufficient to lead to fairly distinct behavior for the two models.

The polarizable models have a more cohesive bulk-liquid phase than the nonpolarizable models, as is discussed in greater detail in Section III.C. Furthermore, the increased cohesion of bulk water for the polarizable models regulates the extent to which water enters the confined region. In the case of TIP4P-FQ, the model with the strongest liquid–liquid interaction, the least amount of water is able to enter (or at least remain in) the confined region at near-critical distances. This has implications for the potential of mean force of hydrophobe dimerization as will be discussed below. It is also relevant to note that the isothermal compressibility of TIP4P-FQ is underestimated ($\kappa_{T=298K} = 38 \pm 2 \times 10^{-6} \text{ bar}^{-1}$ ⁸⁸ relative to experiment ($\kappa_{T=298K} = 45.3 \times 10^{-6} \text{ bar}^{-1}$) and lower than nonpolarizable models (63 ± 5 , 59 ± 5 , and $46.1 \times 10^{-6} \text{ bar}^{-1}$ for TIP3P,⁸⁹ TIP4P,⁸⁹ and SPC/E,⁹⁰ respectively) and SWM4-NDP ($41 \pm 3 \times 10^{-6} \text{ bar}^{-1}$). This suggests that TIP4P-FQ can not accommodate enhanced densities in the confined regions as much as the other models, further supporting the lower interior water count compared to the count for nonpolarizable models at the same

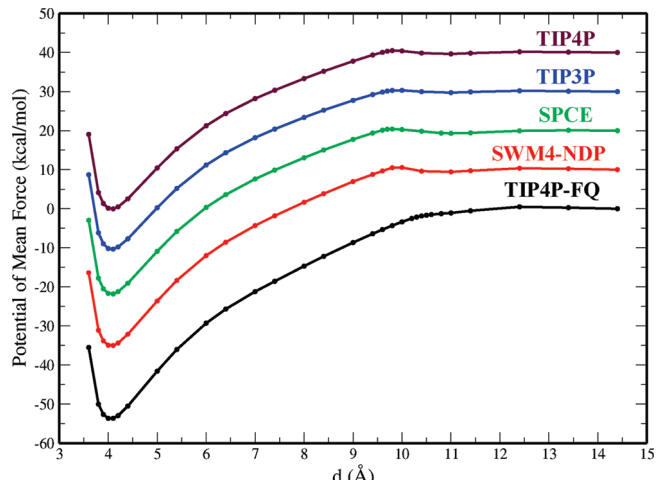


Figure 6. Potential of mean force (PMF) for the dimerization of carbon plates in SPC/E, TIP3P, TIP4P, TIP4P-FQ, and SWM4-NDP water models. A vertical offset of 10 kcal/mol is imposed for each model.

distance. We note, however, that the isothermal compressibility is unlikely to be a primary factor influencing the critical distance since the nonpolarizable models and SWM4-NDP have similar critical distances despite significant differences in their compressibilities.

B. Potential of Mean Force. The potential of mean force (PMF) was computed from the average force acting on each plate at a given separation distance. The profile of average force along the axis of separation was integrated to obtain the PMFs shown in Figure 6. To validate our protocol using an interfacial system within the NVT ensemble (as opposed to the NPT simulations used in earlier work²⁴), we consider that our PMF for the plates in SPC/E water reproduces the result of Zangi et al. within the uncertainty of our calculation. We next consider aspects of the various PMFs of Figure 6. The well depths of the PMF (between the dissociated state at $d = 14.4$ Å and the associated/contact state $d = 4.1$ Å) are summarized in Table 2. We estimate well depths of $-40(\pm 3)$, $-40(\pm 2)$, $-42(\pm 3)$, $-45(\pm 5)$, and $-54(\pm 5)$ kcal/mol for TIP4P, TIP3P, SPC/E, SWM4-NDP, and TIP4P-FQ, respectively. Error bars are

TABLE 2: Selected Properties of the Water Models Used in This Study^a

model	PMF well depth (kcal/mol)	$\langle \mu_{\text{liq}} \rangle$ (Debye)	E_{pol} (kcal/mol)	D_s (10^{-5} cm 2 /s)	d_c (Å)
TIP3P	40(±2)	2.35	0.00	5.1	9.8
TIP4P	40(±3)	2.18	0.00	3.3	9.9
SPC/E	42(±3)	2.35	1.25	2.5	9.7
SWM4-NDP	45(±5)	2.46	2.75	2.30(±0.04)	9.9
TIP4P-FQ	54(±3)	2.62	5.7	1.9(±0.1)	10.5

^a Potential of mean force well depth and critical distance for wetting/dewetting transition (d_c) are results from this study. Average liquid phase dipole moments, self-diffusion constants, and self-polarization energies are taken (or calculated) from the literature (refs 63, 70, 81, 82, and 91).

estimated by integrating the high and low estimates of the forces at each separation (determined by adding or subtracting the standard deviation of forces at each distance to the average value); the average difference from the well depth at these upper and lower bounds to the mean well depth was taken as the uncertainty. Due to less sampling (1–10 ns for some windows relative to other models studied), SWM4-NDP carries higher uncertainty on the forces at the noncritical distances (generally 2–4 times that for other models), resulting in larger uncertainty for the well depth (±5 kcal/mol). Reiterating that interactions involving the plates are parametrized to be equivalent across all systems studied, differences in the potentials of mean force for different water models are influenced by the solvent. We calculate the solvent-induced potential of mean force by subtracting the change in enthalpy associated with plate association ($\Delta H_{\text{plate-association}} = H_{d=4.1\text{\AA}} - H_{d=14.4\text{\AA}} = -16.8$ kcal/mol) from the PMF well depth. Upon such analysis, we note that, relative to the solvent-induced energy associated with plate dimerization for TIP3P and TIP4P, TIP4P-FQ is enhanced by approximately 61%, while SWM4-NDP and SPC/E are enhanced to a lesser extent by 22% and 9%, respectively.

Among the models that are not explicitly polarizable (TIP3P, TIP4P, SPC/E), the SPC/E water model shows the strongest hydrophobic interaction. This correlates with the enhanced self-interactions of bulk water molecules (parametrized in a mean-field manner into the water model to account for self-polarization energy). SPC/E water thus binds more favorably with itself in the bulk relative to the other nonpolarizable water models. This effect also underlies the interactions within the polarizable solvents; the potential influence of the water model's self-polarization energy on hydrophobic association is discussed in the next section. Additionally, analysis of the correlation between the forces on the plates and the number of waters between the plates (not shown) suggests that higher interior densities oppose the dimerization of the plates (at least for distances below or near d_c), whereas less filled states lead to more favorable attraction. This observation supports the differences in the PMFs for the different models. Figure 5a shows that there are generally more water molecules between plates for the nonpolarizable models than the polarizable models at a given distance. This leads to the less favorable interaction between plates in the nonpolarizable water models.

Another distinguishing feature of the profiles is the free energy barrier opposing dimerization. This barrier represents a kinetic restriction on the filling and unfilling of the interior. Similar barriers that distinguish contact and solvent-separated interactions are commonly observed for the association of small hydrophobic solutes.^{6,17,33} The PMFs for the nonpolarizable models and the polarizable SWM4-NDP model exhibit this

roughly 1 kcal/mol barrier near the critical distance. Unlike these models, TIP4P-FQ lacks a pronounced barrier for hydrophobic association. Considering fluctuations of water density between plates from filled and unfilled states, TIP4P-FQ exhibits more rapid transitions between filled and unfilled states as evidenced in part by a more gradual increase of the interior density profile and larger plate separation distance range showing bimodal distributions (Figure 5b). Rick and Berne have previously investigated the association of methane molecules in TIP4P-FQ solvent.⁴² Similar to the results of the large hydrophobe association in the current study, the authors observed a reduced barrier for the small hydrophobe association (at $T = 298$ K) relative to nonpolarizable water results. Interestingly, at higher and lower temperatures ($T = 313$ K and $T = 283$ K, respectively) the barrier is enhanced for the small hydrophobes. It would be informative to investigate the temperature dependence of the large-scale hydrophobe PMF in TIP4P-FQ solvent, although such analysis is beyond the scope of the current work; future studies will address this aspect.

C. Dipole Moment Profiles. One facet of polarizable models that is inherently dissimilar to nonpolarizable models is the ability to dynamically induce a dipole moment. This difference necessitates the enhanced dipole moment of nonpolarizable water models (relative to the experimental gas-phase value) for use in condensed-phase simulations. The nonpolarizable three-site models (SPC/E and TIP3P) have similar dipole moments of about 2.35 D; the four-site TIP4P model possesses a slightly reduced value of 2.18 D. Polarizable models, however, are parametrized to capture the experimental gas phase dipole moment of 1.85 D in vacuum while inducing larger dipole moments in the bulk ($\langle \mu_{\text{avg.}} \rangle = 2.62$ D for TIP4P-FQ and $\langle \mu_{\text{avg.}} \rangle = 2.46$ D for SWM4-NDP). This variation is important for the present study since the region between plates achieves vapor-like densities for plate separations below the critical distance. We consider the dipole moment profiles in Figure 7 for TIP4P-FQ and SWM4-NDP. Panels a and b demonstrate an increased average dipole moment as a function of z -position. It is evident that the dipole moment drops from the bulk value in the region approaching the plates. The variation between gas-phase and bulk dipole moments is larger for TIP4P-FQ than SWM4-NDP ($\Delta\mu = 0.76$ D versus $\Delta\mu = 0.61$ D).

A limitation in the z -dependent profiles is the disruption in the path of a molecule from bulk to interior due to the excluded volume of the plates. Therefore, it is also informative to consider the average dipole moment in the lateral (y) direction, which allows for the direct transition from bulk to interior. For this analysis, a rectangular region ($x \times y \times z$) was sampled. Here $x = 16$ Å (approximately the plate diameter), $y = 36$ Å (the entire width of the simulation cell), and $z = d$ (the plate–plate separation distance); due to the symmetry of the system, we expect similar results if the x -profile was considered. At small plate–plate distances ($d < 7$ Å), the solvent accessible volume between plates is not sufficient to accommodate water molecules in the range of the plate (-8 Å $< y < 8$ Å). With distances above 7 Å, water is first able to enter the interior. For $d = 8.4$ Å, TIP4P-FQ shows an average dipole moment of about 2.3 D, while SWM4-NDP has an average dipole moment between 2.1 and 2.2 D. These dipole moments are of the same order of magnitude as those of water molecules in small clusters, suggesting water entering the hydrophobic cavity prefers to remain partially coordinated. This is further supported through the hydrogen bonding profiles discussed in Section III.D. The profiles for panels c and d do not approach the bulk values for the largest separation due to the contributions to the local

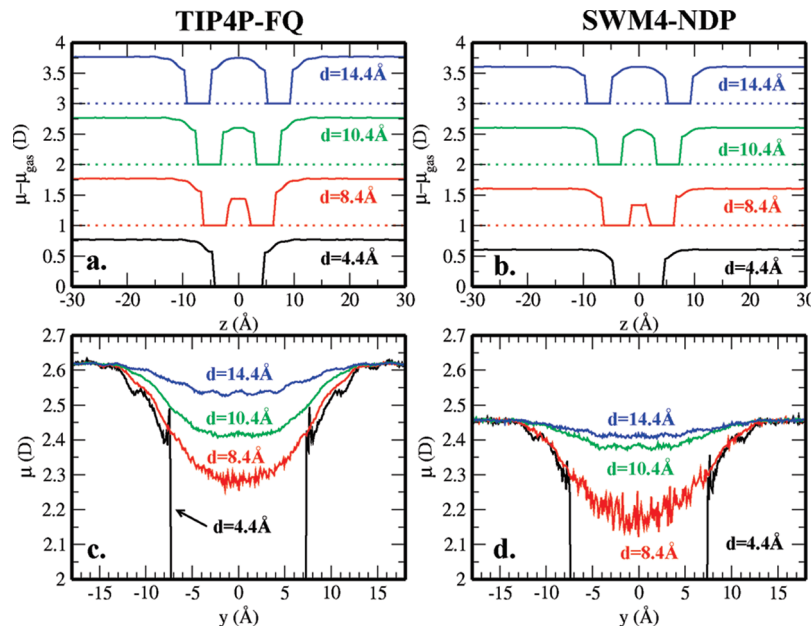


Figure 7. Dipole moment profiles for polarizable water models over a range of plate separation distances. Panels a and b demonstrate the dipole moment enhancement over the gas-phase value for each TIP4P-FQ and SWM4-NDP (respectively) along the z-axis (perpendicular to the plate–water interface). Dipole moment profiles in the y-direction (parallel to the plate–water interface) are shown in c–d.

average dipole moment from water molecules close to the plates, whose dipole moments are lower (as seen in panels a and b). Excluding those waters near the plates would lead to profiles consistent with panels a and b. Panels c and d clearly demonstrate the ability of TIP4P-FQ water to accommodate a broader range of dipole moments compared to the SWM4-NDP force field. This allows for a broader range of plate separations where filled and unfilled states are equally stable (Figure 4b), giving rise to bimodal density distributions over a bigger separation range for TIP4P-FQ.

Water models parametrized to treat polarizability (either explicitly as in the case of TIP4P-FQ and SWM4-NDP or implicitly in the case of SPC/E) feature a correction for the difference in polarization self-energy for a molecule in liquid versus vacuum. This self-polarization energy is positive, requiring a more favorable liquid interaction to reproduce the experimental vaporization enthalpy (vis-a-vis cohesive self-energy) of water. The self-polarization energy can be calculated from the following expression^{63,82}

$$\Delta E_{\text{pol}} = \frac{(\mu_{\text{liq}} - \mu_{\text{gas}})^2}{2\alpha} \quad (4)$$

where α is the polarizability. The self-polarization for SPC/E (1.25 kcal/mol) corresponds to the energy required to induce a dipole from $\mu = 1.85$ D to $\mu = 2.35$ D. Similarly, a self-polarization energy of 2.75 kcal/mol can be calculated for SWM4-NDP based on its polarizability of 0.97825 \AA^3 and an average induced dipole of 0.61 D. Rick, Stuart, and Berne calculated a 5.7 kcal/mol contribution of the self-polarization term for TIP4P-FQ based on the difference in the self-energy for a water molecule in the liquid and gas phases⁶³

$$\Delta E_{\text{pol}} = \langle E(Q^{\text{liq}}) \rangle - E(Q^{\text{gas}}) \quad (5)$$

We consider the relationship between the self-polarization energy for each water model and the calculated well depth from

the PMF for plate association in Figure 8a. The nonpolarizable potentials TIP4P and TIP3P which do not consider the self-polarization energy demonstrate the least favorable association of plates. SPC/E, which incorporates a 1.25 kcal/mol polarization contribution, accommodates a more cohesive liquid–liquid interaction than the other nonpolarizable models. Consequently, SPC/E also exhibits a more favorable well depth for the plate dimerization. This relationship between strength of hydrophobic association and self-polarizability is more apparent in the case of the self-consistently polarizable models, SWM4-NDP and TIP4P-FQ. These models have larger self-polarization corrections and more favorable well depths than SPC/E. In a similar analysis, we compare the relationship between magnitude of the induced dipole moment and PMF well-depth (Figure 8b). TIP3P and TIP4P were assigned values of $\mu^{\text{induced}} = 0$ D since they do not, either explicitly or implicitly, contain a self-polarization energy correction; SPC/E was assigned an induced dipole moment of 0.5 D, corresponding to its self-polarization energy. Here the trend of increasing well depth magnitude with increasing induced dipole moment is also evident, which is anticipated due to the relationship between magnitude of the induced dipole moment and self-polarization energy.

Indeed, models that treat polarizability either implicitly (in the case of SPC/E) or explicitly (SWM4-NDP and TIP4P-FQ) account for stronger water–water interactions, thereby increasing the driving force for hydrophobic assembly. This self-interaction also correlates with the diffusion properties of pure water. For instance, the self-diffusion constants of TIP4P and TIP3P (3.3 and $5.1 \times 10^{-5} \text{ cm}^2/\text{s}$, respectively)⁹¹ overestimate experiment ($2.3 \times 10^{-5} \text{ cm}^2/\text{s}$), whereas the other models more accurately predict this quantity. In this context, TIP4P-FQ which underestimates the self-diffusion constant (1.9 versus $2.3 \times 10^{-5} \text{ cm}^2/\text{s}$)⁶³ has the strongest liquid water interaction and the highest self-polarization energy (5.7 kcal/mol). It is possible that TIP4P-FQ induces too large of a hydrophobic interaction, and the TIP4P-FQ result can be considered a limiting case. The nature of condensed phase dipole moments of water, despite a long history of research, is still not fully quantified.^{92–96}

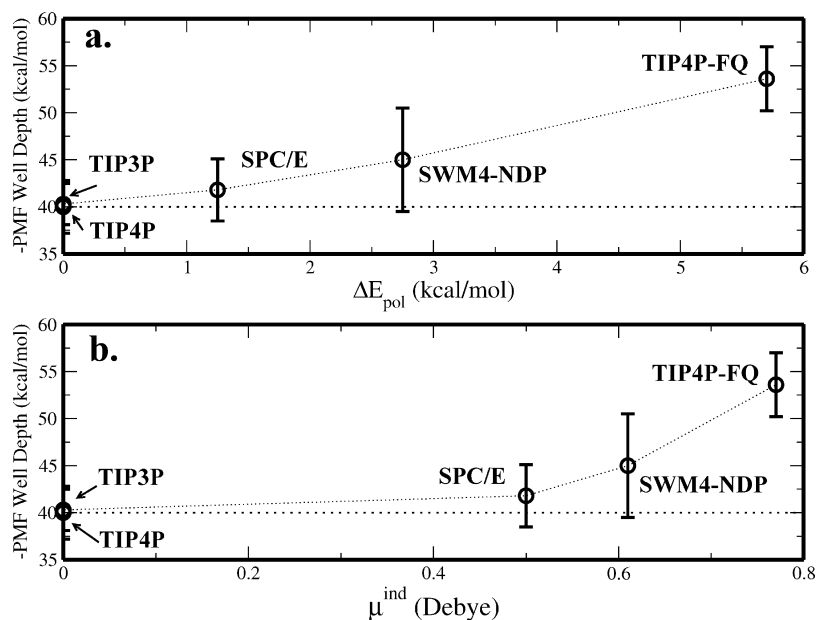


Figure 8. (a) Relationship between the self-polarization energy and the PMF well depth. (b) Well depth of the PMF versus the average induced dipole moment for each water model. SPC/E, although a fixed charge model, implicitly includes a self-polarization contribution of 1.25 kcal/mol, corresponding to an average induced dipole moment of 0.5 D. This distinguishes SPC/E from the other fixed charge models (TIP3P and TIP4P) which feature no self-polarization correction or induced dipole moment. In each panel, a horizontal line at 40 kcal/mol (the approximate well depth of TIP3P and TIP4P) is included as a visual guide.

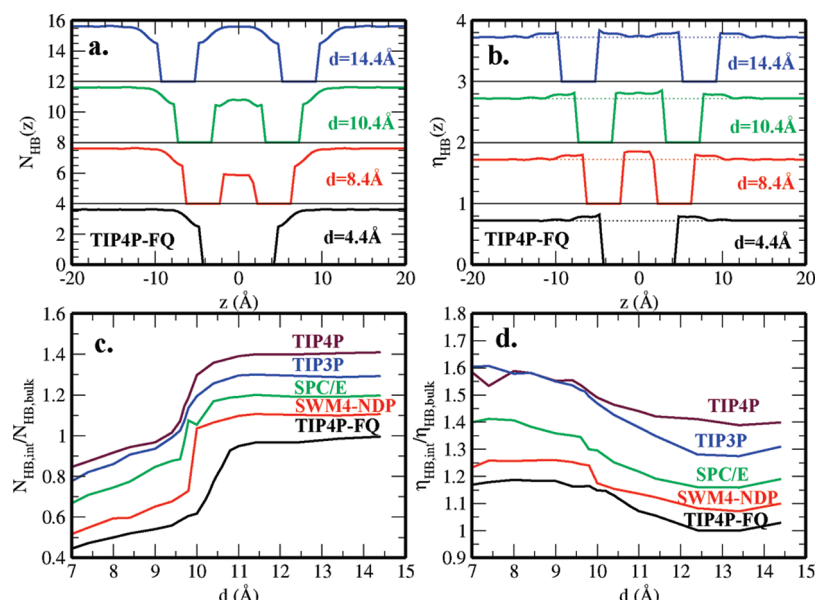


Figure 9. Hydrogen bond profiles. (a) The average number of hydrogen bonds per TIP4P-FQ water molecule as a function of its z -position for varying plate–plate separation distances. (b) The average efficiency of hydrogen bonding for a TIP4P-FQ water molecule as a function of z -position. (c) The number of hydrogen bonds between plates ($z = 0 \text{ \AA}$) relative to the average bulk value for the water models studied at various distances. (d) Efficiency of hydrogen bonding (relative to bulk) between plates at various distances. Vertical offsets of 4, 1, 0.1, and 0.1 were imposed for panels a–d, respectively.

D. Hydrogen Bond Profiles. Two water molecules were considered to be hydrogen bonded if the oxygen–oxygen distance is less than 3.5 \AA and the OOH angle is less than 30°.⁹⁷ We define efficiency η_{HB} of a hydrogen bond as the number of hydrogen bonds formed by a molecule divided by the coordination number of the water molecule, which includes all water molecules satisfying only the distance criterion. The hydrogen bond profiles are shown in Figure 9. The average number of hydrogen bonds and the average efficiency of hydrogen bonding for TIP4P-FQ are shown in Figure 9a and b for various plate separation distances. In the vicinity of the hydrophobic plates, the average number of hydrogen bonds monotonically decreases,

but the efficiency is enhanced relative to the bulk value in the region corresponding to the initial drop in hydrogen bond number. This behavior is similar to that observed at the liquid–vapor interface.^{97,98} The water between plates is of particular interest. At low plate separation distances, the number of hydrogen bonds is reduced; this result is expected based on the limited capacity for water to be coordinated due to the spatial constraints in this confined region. This is further manifested in the increased efficiency of hydrogen bonding between the plates. As the plate–plate separation distance approaches the dissociated state, the average number of hydrogen bonds, as well as the efficiency of hydrogen bonding, approaches the bulk

values. In the context of dewetting–wetting transitions, analysis of hydrogen bonding between plates is insightful. We consider the average number of hydrogen bonds and the average efficiency of hydrogen bonding between the plates (more specifically at $z = 0 \text{ \AA}$, where water is equidistant to both plates) for each water model as a function of plate separation distance, d , in Figure 9c,d. The average number of hydrogen bonds between plates (panel c) demonstrates similar qualitative behavior as the average number of water molecules confined between plates as a function of separation (Figure 5a).

At small plate–plate separation distances (corresponding to those in which water is first able to enter the confined region, i.e., $d \approx 7.0 \text{ \AA}$), water molecules tend to form half as many hydrogen bonds as they do in bulk liquid. However, hydrogen bond efficiency is enhanced relative to the condensed phase. This is explained by the reduced coordination of these interior water molecules while maintaining hydrogen bonding to reduce enthalpically unfavorable isolated molecules. We see for all models that the efficiency in hydrogen bonding decreases going from close plate–plate distances to near critical distances and ultimately approaches bulk hydrogen bonding efficiency at dissociated plate–plate distances. The efficiency reduction near the critical distance may be the result of altered diffusive properties. As discussed by Chowdhary et al.,⁹⁹ reduced translational diffusion near hydrophobic interfaces (relative to the bulk) allows for water to reform hydrogen bonds and ultimately increases the time required to relax a hydrogen bond. Another recent study⁵⁴ observed reduced diffusion rates when water was confined between large hydrophobes (at a distance allowing one interior water layer). This was attributed to the influence of the local topography of the confining surface on confined water diffusion. For the current study, the reduced hydrogen bond efficiency with increasing plate distances can be associated to faster translational diffusion made possible by increased confined volume (at z -positions equidistant from both plates) that is not directly influenced by surface effects. With such increased translational diffusion, hydrogen bonds are less able to reform, thus reducing the efficiency of hydrogen bonding in the confined region at $z = 0 \text{ \AA}$. The efficiency of hydrogen bonding at the water/plate interface, however, is relatively unaffected by plate separation distance (it remains enhanced relative to bulk).

E. Orientation. We consider the number densities of hydrogen and oxygen atoms as a function of their z -position in Figure 10a. The hydrogen density extends beyond the oxygen density in the vicinity of the plates, suggesting the water molecules orient such that the hydrogen atoms point closer to the plates. This is consistent with the orientation of water at the liquid–vapor interface which allows for maximization of hydrogen bonding; this orientational preference is generally believed to be common to both interfaces.¹⁰ This orientational preference is further examined in the atomic excesses presented in Figure 10b. Here, the average density of oxygen was subtracted from one-half the hydrogen density at each z -position; the one-half factor for hydrogen is included to correct for stoichiometry. Since data in this figure are offset by 0.02 vertical units, a horizontal line is included for each system to indicate the value of no net excess. Values above this line denote an excess of hydrogen at a given position, while values below indicate an excess of oxygen. These profiles demonstrate that all models studied have similar orientational behavior. In the vicinity of the plates, ordered layers of alternating hydrogen and oxygen excess emerge. This structuring persists until

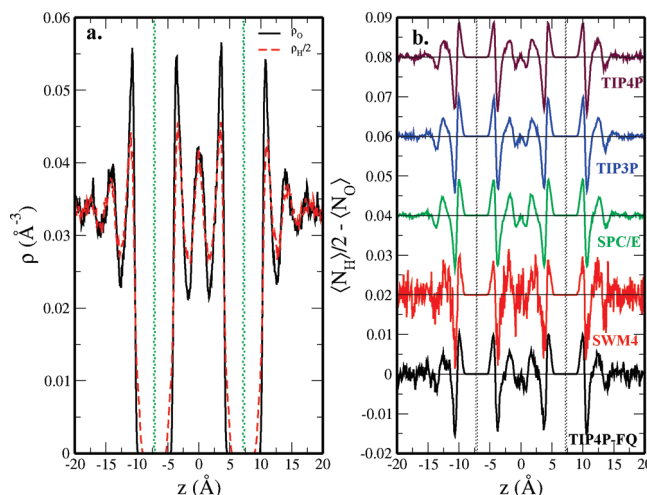


Figure 10. Profiles describing the orientation of water as a function of z -position for plate–plate distances of $d = 14.4 \text{ \AA}$. (a) Number density profiles of oxygen and hydrogen (scaled by one-half) for TIP4P-FQ. (b) Atomic excess for hydrogen and oxygen. A vertical offset of 0.02 units was applied between systems; the horizontal line indicates zero atomic excess (no net orientation). Values above the horizontal line indicate an excess of hydrogen atoms at a given position, and values below it suggest an excess of oxygen at a given position.

distances of about 7 \AA from the plates, after which the average excess approaches zero (suggesting no net orientation).

IV. Discussion and Conclusions

We have presented molecular dynamics simulation results of the potential of mean force between two large hydrophobes with several popular nonpolarizable solvent models as well as two explicitly polarizable solvent models, the TIP4P-FQ and SWM4-NDP models. Regarding the hydrophobic interaction, we observe an unambiguous difference between the hydrophobic interaction strength in the nonpolarizable and polarizable water environments, the stronger interactions occurring in the most polarizable water model, TIP4P-FQ.

The present results suggest significant differences in the condensed phase arising from explicit consideration of solvent polarization. We observe a strong relationship between the self-polarization energy and strength of hydrophobic interaction. For the nonpolarizable water models, we observe almost identical PMF depths regardless of the magnitude of the condensed phase dipole moment. For the polarizable models, the hydrophobic interaction strength is modulated by the polarization of the solvent. Comparing the several water models utilized in this study, we see that the explicitly polarizable water models are effectively more cohesive than their nonpolarizable counterparts. The additional cohesive energy in the condensed phase arises in response to the positive self-polarization energy. In the case of TIP4P-FQ, the self-polarization energy is 5.7 kcal/mol; for the SWM4-NDP model, the self-polarization is 2.75 kcal/mol. Incidentally, the SPC/E model, though not explicitly polarizable as the other models, incorporates the polarization self-energy ($E_{\text{pol}} = 1.25 \text{ kcal/mol}$) based on a condensed phase dipole moment of water of 2.35 D. Thus, it too possesses a more cohesive bulk interaction relative to the nonpolarizable water models. As such, the relative ordering of the hydrophobic effect, as embodied in the plate–plate interaction PMF well-depth, is TIP4P-FQ > SWM4-NDP > SPC/E. It is difficult to comment on the accuracy of the models in terms of how well each captures the condensed phase cohesiveness. This is in large part due to the ambiguity of knowing the *true* condensed phase

dipole moment of a water molecule. There have been numerous values of this property stated in the literature.^{92–96} However, each has important caveats to contend with. Suffice it to say that further efforts to more specifically define this value are warranted. In the final analysis, we reiterate that polarization does have a significant influence in inhomogeneous environments, in this case relating particularly to the hydrophobic association of large hydrophobes. Although earlier studies^{5,38,41,42} examined the role of solvent polarizabilities in the hydration of methane molecules, these studies did not use the same interactions for methane. Consequently, different results were obtained regarding whether the methane–methane contact pair or the solvent-separated pair was favorable. The more recent study of Rick and Berne suggested inclusion of solvent polarizability led to only minor differences from nonpolarizable models.⁴² Few subsequent studies incorporating solvent polarizability to address hydrophobic effects have appeared in the literature. Indeed, the current work suggests polarizability is an important consideration when studying large-scale hydrophobes or water under hydrophobic confinement. The implications relate to the folding rates (kinetics) of proteins or the time scales of hydrophobic association.

We also observed similarities between properties at the water–hydrophobe interface and the water–vapor interface. The extent of density fluctuations near the water–hydrophobe interfaces is enhanced over the fluctuations in bulk by a factor of approximately 1.2. Such an enhancement seems modest compared to significant tails in probability distributions as seen in earlier studies.^{45,46} However, the treatment of dispersive forces (as in the present study) results in more bulklike distributions and fluctuations (for example, see Figure 4a of ref 46). Unlike the liquid–vapor interface, however, average density profiles in the vicinity of the water–hydrophobe interface show enhancement and a density layering. Such differences arise from the water–hydrophobe dispersion interaction and the smoothness of the hydrophobic surface as has been discussed in previous studies.^{9,45,46} Orientation of water near the hydrophobic plates also mimics that near the liquid–vapor interface, with hydrogen atoms penetrating closer toward the plate than the oxygen atoms. Such an orientation minimizes the disruption to hydrogen bonding near the plates, thus reducing the enthalpic penalty for solvating the plates. Consistent with this observation, the efficiency of hydrogen bonding near the plates is enhanced near the plates as it is at the liquid–vapor interface.^{97,98} Although we consider hydrogen bonding at a static level, the dynamics of hydrogen bonding in the vicinity of the plates or confined between the plates would be insightful. Recent simulations have begun to examine such effects. In a study of hydrogen bond dynamics for SPC/E at the water/liquid hydrocarbon interface,⁹⁹ the rate of hydrogen bond breaking was increased relative to the bulk. However, this effect is masked by an increased rate of hydrogen bond reformation (made possible by reduced translational diffusion normal to the interface) which ultimately results in longer relaxation time for interfacial water.⁹⁹ More recently, the translational and vibrational dynamics of water confined between hydrophobic solutes has been examined.⁵⁴ Choudhury observed significant changes in translational and rotational dynamics with changes in the topology of the hydrophobe. Notably, translational diffusion of confined water is shown to be reduced at small intermolecular distances due to the influence of surface topology; at intermolecular distances capable of accommodating two or more layers of water, such topology effects are not observed, and faster translational diffusion results.⁵⁴ Furthermore, liquid–vapor interfacial simula-

tions by Liu et al.⁹⁷ demonstrate significantly enhanced diffusion at the interface (2–4 times the bulk value) for TIP4P-FQ. They point out that reduced polarization of this model approaching vapor effectively weakens the pair interaction and enhances the rate of diffusion (to a greater extent than nonpolarizable models). Certainly, the water models used in this work have different diffusion properties, and a systematic study of the diffusional, rotational, and hydrogen bond dynamics among these models would further explain the observed differences in their wetting/dewetting transitions.

In this study, we consider pure water at ambient conditions. However, additives such as urea¹⁰⁰ or Hofmeister series salts,^{83,101–104} pressure,^{49,105} temperature,^{24,42,106} the presence of interfaces,¹⁰⁷ and length-scale of hydrophobic solutes^{21,108,109} can influence the behavior of hydrophobic interactions. It would be insightful to examine the effect of polarizability under such variable conditions. Furthermore, studies investigating the mechanism driving the wetting/dewetting transition of water under confinement would enhance our understanding of the limiting kinetics for hydrophobically driven processes.

Acknowledgment. The authors acknowledge support from the National Institutes of Health (COBRE:5P20RR017716-07) at the University of Delaware, Department of Chemistry and Biochemistry.

References and Notes

- (1) Kauzmann, W. *Adv. Protein Chem.* **1959**, *14*, 1–63.
- (2) Dill, K. A. *Biochemistry* **1990**, *29*, 7133–7155.
- (3) Nagarajan, R.; Ruckenstein, E. *Langmuir* **1991**, *7*, 2934–2969.
- (4) Stillinger, F. H. J. *Solution Chem.* **1973**, *2*, 141–158.
- (5) Pratt, L. R. *Annu. Rev. Phys. Chem.* **2002**, *53*, 409–436.
- (6) Southall, N. T.; Dill, K. A.; Haymet, A. D. J. *J. Phys. Chem. B* **2002**, *106*, 521–533.
- (7) Tanford, C. *J. Am. Chem. Soc.* **1962**, *84*, 4240–4247.
- (8) Tanford, C. *Protein Sci.* **1997**, *6*, 1358–1366.
- (9) Pratt, L. R.; Pohorille, A. *Chem. Rev.* **2002**, *102*, 2671–2692.
- (10) Berne, B. J.; Weeks, J. D.; Zhou, R. *Annu. Rev. Phys. Chem.* **2009**, *60*, 85–103.
- (11) Chandler, D. *Nature* **2005**, *437*, 640–647.
- (12) Rasaiyah, J. C.; Garde, S.; Hummer, G. *Annu. Rev. Phys. Chem.* **2008**, *59*, 713–740.
- (13) Widom, B.; Bhimalapuram, P.; Koga, K. *Phys. Chem. Chem. Phys.* **2003**, *5*, 3085–3093.
- (14) Baldwin, R. L. *Proc. Natl. Acad. Sci.* **1986**, *83*, 8069–8072.
- (15) Granick, S.; Bae, S. C. *Science* **2008**, *322*, 1477–1478.
- (16) Huang, D. M.; Chandler, D. *Proc. Natl. Acad. Sci.* **2000**, *97*, 8324–8327.
- (17) Hummer, G.; Garde, S.; Garcia, A. E.; Paulaitis, M. E.; Pratt, L. R. *J. Phys. Chem. B* **1998**, *102*, 10469–10482.
- (18) Hummer, G.; Garde, S. *Phys. Rev. Lett.* **1998**, *80*, 4193–4196.
- (19) Hummer, G.; Garde, S.; Garcia, A. E.; Pratt, L. R. *Chem. Phys.* **2000**, *258*, 349–370.
- (20) Hummer, G.; Rassiah, J. C.; Noworyta, J. P. *Nature* **2001**, *414*, 188–190.
- (21) Lum, K.; Chandler, D.; Weeks, J. D. *J. Phys. Chem. B* **1999**, *103*, 4570–4577.
- (22) Pratt, L. R.; Chandler, D. *J. Chem. Phys.* **1977**, *67*, 3683–3704.
- (23) Pratt, L. R.; Chandler, D. *J. Chem. Phys.* **1980**, *73*, 3430–3433.
- (24) Zangi, R.; Berne, B. *J. Phys. Chem. B* **2008**, *112*, 8634–8644.
- (25) Hummer, G.; Garde, S.; Garcia, A. E.; Pohorille, A.; Pratt, L. R. *Proc. Natl. Acad. Sci.* **1996**, *93*, 8951–8955.
- (26) Berne, B. J. *Proc. Natl. Acad. Sci.* **1996**, *93*, 8800–8803.
- (27) Wallqvist, A.; Gallicchio, E.; Levy, R. M. *J. Phys. Chem. B* **2001**, *105*, 6745–6753.
- (28) Graziano, G. *J. Phys. Chem. B* **2009**, *113*, 11232–11239.
- (29) Luzar, A.; Leung, K. *J. Chem. Phys.* **2000**, *113*, 5836–5844.
- (30) Lum, K.; Luzar, A. *Phys. Rev. E* **1997**, *56*, R6283.
- (31) Sarupria, S.; Garde, S. *Phys. Rev. Lett.* **2009**, *103*, 037803.
- (32) Vaitheswaran, S.; Yin, H.; Rasaiyah, J. C.; Hummer, G. *Proc. Natl. Acad. Sci.* **2004**, *101*, 17002–17005.
- (33) Zhu, S.; Elcock, A. H. *J. Chem. Theory Comput.* **2010**, *6*, ASAP Article.
- (34) Ashbaugh, H. S.; Collett, N. J.; Hatch, H. W.; Staton, J. A. *J. Chem. Phys.* **2010**, *132*, 124504.

- (35) Geiger, A.; Rahman, A.; Stillinger, F. H. *J. Chem. Phys.* **1978**, *70*, 263–276.
- (36) Pangali, C.; Rao, M.; Berne, B. *J. J. Chem. Phys.* **1979**, *71*, 2975–2981.
- (37) Pangali, C.; Rao, M.; Berne, B. *J. J. Chem. Phys.* **1979**, *71*, 2982–2990.
- (38) van Belle, D.; Wodak, S. *J. J. Am. Chem. Soc.* **1993**, *115*, 647–652.
- (39) Smith, D. E.; Haymet, A. D. *J. J. Chem. Phys.* **1993**, *98*, 6445–6454.
- (40) Dang, L. X. *J. Chem. Phys.* **1994**, *100*, 9032–9034.
- (41) New, M. H.; Berne, B. *J. J. Am. Chem. Soc.* **1995**, *117*, 7172–7179.
- (42) Rick, S. W.; Berne, B. *J. J. Phys. Chem. B* **1997**, *101*, 10488–10493.
- (43) Young, W. S.; Brooks, C. L., III. *J. Chem. Phys.* **1997**, *106*, 9265–9269.
- (44) Willard, A. P.; Chandler, D. *J. Phys. Chem. B* **2008**, *112*, 6187–6192.
- (45) Godawat, R.; Jamadagni, S. N.; Garde, S. *Proc. Natl. Acad. Sci.* **2009**, *106*, 15119–15124.
- (46) Patel, A. J.; Varilly, P.; Chandler, D. *J. Phys. Chem. B* **2010**, *114*, 1632–1637.
- (47) Mittal, J.; Hummer, G. *Proc. Natl. Acad. Sci.* **2008**, *105*, 20130–20135.
- (48) Wallqvist, A.; Berne, B. *J. J. Phys. Chem.* **1995**, *99*, 2885–2892.
- (49) Giovambattista, N.; Rossky, P. J.; Debenedetti, P. G. *Phys. Rev. E* **2006**, *73*, 041604.
- (50) Kumar, P.; Buldyrev, S. V.; Starr, F. W.; Giovambattista, N.; Stanley, H. *E. Phys. Rev. E* **2005**, *72*, 051503.
- (51) Huang, X.; Margulis, C. J.; Berne, B. *J. Proc. Natl. Acad. Sci.* **2003**, *100*, 11953–11958.
- (52) Hua, L.; Zangi, R.; Berne, B. *J. J. Phys. Chem. C* **2009**, *113*, 5244–5253.
- (53) Gordillo, M. C.; Nagy, G.; Marti, J. *J. Chem. Phys.* **2005**, *123*, 054707.
- (54) Choudhury, N. *J. Chem. Phys.* **2010**, *132*, 064505.
- (55) Berezhkovskii, A.; Hummer, G. *Phys. Rev. Lett.* **2002**, *89*, 064503.
- (56) Setny, P.; Wang, Z.; Cheng, L.; Li, B.; McCammon, J. A.; Dzubiella, J. *Phys. Rev. Lett.* **2009**, *103*, 187801.
- (57) Ewell, J.; Gibb, B. C.; Rick, S. W. *J. Phys. Chem. B* **2008**, *112*, 10272–10279.
- (58) Werder, T.; Walther, J. H.; Jaffe, R. L.; Halicioglu, T.; Koumoutsakos, P. *J. Phys. Chem. B* **2003**, *107*, 1345–1352.
- (59) Kathmann, S. M.; Kuo, I. W.; Mundy, C. J. *J. Am. Chem. Soc.* **2008**, *130*, 16556–16561.
- (60) Kathmann, S. M.; Kuo, I. W.; Mundy, C. J. *J. Am. Chem. Soc.* **2009**, *131*, 17522.
- (61) Krishnal, A.; Senet, P.; Yang, M.; Van Alsenoy, C. *J. Chem. Phys.* **2006**, *125*, 034312.
- (62) Rappe, A. K.; Goddard, W. A. *J. Phys. Chem.* **1991**, *95*, 3358–3363.
- (63) Rick, S. W.; Stuart, S. J.; Berne, B. *J. J. Chem. Phys.* **1994**, *101*, 6141–6156.
- (64) Rick, S. W.; Stuart, S. J.; Bader, J. S.; Berne, B. *J. J. Mol. Liq.* **1995**, *65/66*, 31.
- (65) Patel, S.; Brooks, C. L., III. *J. Comput. Chem.* **2004**, *25*, 1–15.
- (66) Patel, S.; MacKerell, A. D., Jr.; Brooks, C. L., III. *J. Comput. Chem.* **2004**, *25*, 1504–1514.
- (67) Patel, S.; Brooks, C. L., III. *Mol. Simul.* **2006**, *32*, 231–249.
- (68) Lamoureux, G.; Roux, B. *J. Chem. Phys.* **2003**, *119*, 3025.
- (69) Lamoureux, G.; MacKerell, A. D., Jr.; Roux, B. *J. Chem. Phys.* **2003**, *119*, 5185.
- (70) Lamoureux, G.; Harder, E.; Vorobyov, I. V.; Roux, B.; MacKerell, A. D., Jr. *Chem. Phys. Lett.* **2006**, *418*, 245–249.
- (71) Lopes, P. E. M.; Lamoureux, G.; Roux, B.; MacKerell, A. D., Jr. *J. Phys. Chem. B* **2007**, *111*, 2873–2885.
- (72) Anisimov, V. M.; Lamoureux, G.; Vorobyov, I. V.; Huang, N.; Roux, B., Jr. *J. Chem. Theory Comput.* **2005**, *1*, 153–168.
- (73) Yu, H.; Whitfield, T. W.; Harder, E.; Lamoureux, G.; Vorobyov, I.; Anisimov, V. M.; MacKerell, A. D., Jr.; Roux, B. *J. Chem. Theory Comput.* **2010**, *6*, 774–786.
- (74) Applequist, J.; Carl, J. R.; Fung, K. *J. Am. Chem. Soc.* **1972**, *94*, 2952–2960.
- (75) Thole, B. T. *Chem. Phys.* **1981**, *59*, 341–350.
- (76) Grossfield, A.; Ren, P.; Ponder, J. W. *J. Am. Chem. Soc.* **2003**, *125*, 15671–15682.
- (77) Ponder, J. W.; Wu, C.; Ren, P.; Pande, V. S.; Chodera, J. D.; Schnieders, M. J.; Haque, I.; Mobley, D. L.; Lambrecht, D. S.; DiStasio, R. A., Jr.; Head-Gordon, M.; Clark, G. N. I.; Johnson, M. E.; Head-Gordon, T. *J. Phys. Chem. B* **2010**, *114*, 2549–2564.
- (78) Ren, P.; Ponder, J. W. *J. Comput. Chem.* **2002**, *23*, 1497–1506.
- (79) Ren, P.; Ponder, J. W. *J. Phys. Chem. B* **2003**, *107*, 5933–5947.
- (80) Brooks, B. R.; et al. *J. Comput. Chem.* **2009**, *30*, 1545–1614.
- (81) Jorgensen, W. L.; Chandrasekhar, J.; Madura, J. D.; Impey, R. W.; Klein, M. L. *J. Chem. Phys.* **1983**, *79*, 926–935.
- (82) Berendsen, H. J. C.; Grigera, J. R.; Straatsma, T. P. *J. Phys. Chem.* **1987**, *91*, 6269–6271.
- (83) Zangi, R.; Hagen, M.; Berne, B. *J. Am. Chem. Soc.* **2007**, *129*, 4678–4686.
- (84) Li, X.; Li, J.; Eleftheriou, M.; Zhou, R. *J. Am. Chem. Soc.* **2006**, *128*, 12439–12447.
- (85) Darden, T.; York, D.; Pedersen, L. *J. Chem. Phys.* **1993**, *98*, 10089–10092.
- (86) Ryckaert, J. P.; Ciccotti, G.; Berendsen, H. J. C. *J. Comput. Phys.* **1977**, *23*, 327–341.
- (87) Nose, S. *Mol. Phys.* **1984**, *52*, 255–268.
- (88) Rick, S. W. *J. Chem. Phys.* **2001**, *114*, 2276–2283.
- (89) Jorgensen, W. L.; Jenson, C. *J. Comput. Chem.* **1998**, *19*, 1179–1186.
- (90) Pi, H. L.; Aragones, J. L.; Vega, C.; Noya, E. G.; Abascal, J. L. F.; Gonzalez, M. A.; McBride, C. *Mol. Phys.* **2009**, *107*, 365–374.
- (91) Jorgensen, W. L.; Tirado-Rives, J. *Proc. Natl. Acad. Sci.* **2005**, *102*, 6665–6670.
- (92) Sprik, M. *J. Chem. Phys.* **1991**, *95*, 6762–6769.
- (93) Kuo, I. W.; Mundy, C. J.; Eggimann, B. L.; McGrath, M. J.; Siepmann, J.; Chen, B.; Vieceli, J.; Tobias, D. *J. J. Phys. Chem. B* **2006**, *110*, 3738–3746.
- (94) McGrath, M. J.; Siepmann, J. I.; Kuo, I. W.; Mundy, C. J. *Mol. Phys.* **2007**, *105*, 1411–1417.
- (95) Silvestrelli, P. L.; Parrinello, M. *Phys. Rev. Lett.* **1999**, *82*, 3308–3311.
- (96) Badyal, Y. S.; Saboungi, M.; Price, D. L.; Shastri, S. D.; Haeffner, D. R.; Soper, A. K. *J. Chem. Phys.* **2000**, *112*, 9206–9208.
- (97) Liu, P.; Harder, E.; Berne, B. *J. J. Phys. Chem. B* **2005**, *109*, 2949–2955.
- (98) Bauer, B. A.; Warren, G. L.; Patel, S. *J. Chem. Theory Comput.* **2009**, *5*, 359–373.
- (99) Chowdhary, J.; Ladanyi, B. M. *J. Phys. Chem. B* **2009**, *113*, 4045–4053.
- (100) Zangi, R.; Zhou, R.; Berne, B. *J. J. Am. Chem. Soc.* **2009**, *131*, 1535–1541.
- (101) Zangi, R. *J. Phys. Chem. B* **2010**, *114*, 643–650.
- (102) Jonsson, M.; Skepo, M.; Linse, P. *J. Phys. Chem. B* **2006**, *110*, 8782–8788.
- (103) Ghosh, T.; Kalra, A.; Garde, S. *J. Phys. Chem. B* **2005**, *109*, 642–651.
- (104) Godawat, R.; Jamadagni, S. N.; Garde, S. *J. Phys. Chem. B* **2010**, *114*, 2246–2254.
- (105) Rick, S. W. *J. Phys. Chem. B* **2000**, *104*, 6884–6888.
- (106) Giovambattista, N.; Rossky, P. J.; Debenedetti, P. G. *J. Phys. Chem. B* **2009**, *113*, 13723–13734.
- (107) Jamadagni, S. N.; Godawat, R.; Dordick, J. S.; Garde, S. *J. Phys. Chem. B* **2009**, *113*, 4093–4101.
- (108) Anthawale, M. V.; Goel, G.; Ghosh, T.; Truskett, T. M.; Garde, S. *Proc. Natl. Acad. Sci.* **2007**, *104*, 733–738.
- (109) Huang, X.; Margulis, C. J.; Berne, B. *J. J. Phys. Chem. B* **2003**, *107*, 11742–11748.